



Polarization in the GG Tau Ring—Confronting Dust Self-scattering, Dust Mechanical and Magnetic Alignment, Spirals, and Dust Grain Drift

Ya-Wen Tang¹ , Anne Dutrey², Patrick M. Koch¹ , Stephane Guilloteau² , Hsi-Wei Yen¹ , Emmanuel di Folco² ,
Eric Pantin³ , Takayuki Muto⁴, Akimasa Kataoka⁵ , and Robert Brauer^{6,7}

¹ Academia Sinica, Institute of Astronomy and Astrophysics, 11F of AS/NTU Astronomy-Mathematics Building, No.1, Sec. 4, Roosevelt Rd., Taipei, Taiwan; ywtang@asiaa.sinica.edu.tw

² Laboratoire d'Astrophysique de Bordeaux, Université de Bordeaux, CNRS, B18N, Allée Geoffroy Saint-Hilaire, F-33615 Pessac, France

³ Laboratoire CEA, IRFU/Dap, AIM, Université Paris-Saclay, Université Paris Diderot, Sorbonne Paris Cité, CNRS, F-91191 Gif-sur-Yvette, France

⁴ Division of Liberal Arts, Kogakuin University, Tokyo, Japan

⁵ National Astronomical Observatory of Japan, Osawa 2-21-1, Mitaka, Tokyo 181-8588, Japan

⁶ Université Paris-Saclay, CNRS, Institut d'Astrophysique Spatiale, F-91405 Orsay, France

⁷ IRFU/SAP Service D'Astrophysique, CEA, Gif-sur-Yvette, France

Received 2022 November 23; revised 2023 March 13; accepted 2023 March 13; published 2023 April 11

Abstract

We report Atacama Large Millimeter/submillimeter Array (ALMA) polarization observations at 3 and 0.9 mm toward the GG Tau A system. In the ring, the percentage is relatively homogeneous at 3 mm, being 1.2%, while it exhibits a clear radial variation at 0.9 mm with a mean increasing from 0.6% to 2.8% toward larger radius (r). The polarization orientation at $r > 1''.85$ appears nearly azimuthal at both wavelengths. At $r < 1''.85$, the pattern remains azimuthal at 3 mm but becomes radial at 0.9 mm. The dust self-scattering model with a_{\max} of 1 mm could reproduce the observed polarization orientation and percentage at 0.9 mm, but the expected polarization percentage at 3 mm would be 0.2%, much smaller than the detected 1.2%. Dust alignment with poloidal magnetic field could qualitatively reproduce the flip in polarization at $r < 1''.85$ and also the detected polarization percentage. A closer inspection of the nearly azimuthal pattern reveals that polarization orientations are systematically deviating by $-9^\circ 0 \pm 1^\circ 2$ from the tangent of the orbit ellipses. This deviation agrees with the direction of the spiral pattern observed in the near-infrared, but it is unclear how dust grains could be aligned along such spirals. For the scenario where the -9° deviation ($-7^\circ 3$ after considering the inclination effect) measures the radial component of the dust drift motion, the expected inward drifting velocity would be $\sim 12.8\%$ of the Keplerian speed, a factor of 2.8 larger than the theoretical predictions. Possible additional interpretations of the polarization are discussed, but there is no single mechanism that could explain the detected polarization simultaneously.

Unified Astronomy Thesaurus concepts: [Interstellar medium \(847\)](#); [Circumstellar disks \(235\)](#)

1. Introduction

The polarization of dust continuum emission at millimeter wavelengths is a powerful way to sample the emitting medium properties. As dust grains are not spherical, the polarization is an indirect tracer of grain alignment mechanisms. The recent Atacama Large Millimeter/submillimeter Array (ALMA) observations at high angular resolution of the circumstellar disk orbiting around HL Tau (Kataoka et al. 2017) showed the complexity of polarization patterns in disks and also revealed the importance of self-scattering. In order to explain polarization in circumstellar disks, several dust grain alignment mechanisms have been recently investigated, including gas-flow alignment (Yang et al. 2018; Kataoka et al. 2019), B field alignment in the Mie regime (Guillet et al. 2020), and radiative alignment (Tazaki et al. 2017). In all cases, polarization is very sensitive to grain sizes.

To reveal the origin of dust polarization, observations of large and bright disks are required, as the polarized intensity is expected to have very low surface brightness. In this respect, the GG Tau A system is an excellent candidate. Located at 150 pc (GAIA collaboration et al. 2018), GG Tau A is surrounded

by a circumtermary Keplerian disk (Di Folco et al. 2014) that consists of a dense ring of gas and dust extending from ~ 190 to 280 au from the central stars and a lower density outer disk extending out to ~ 800 au (e.g., Dutrey et al. 1994; Guilloteau et al. 1999; Piétu et al. 2011). The disk has an inclination angle (i) $\simeq 35^\circ$, with a rotation axis from north to east (PA) of $6^\circ 5$ (Dutrey et al. 2014). The total mass of the disk, $\sim 0.15 M_\odot$ (Dutrey et al. 1994), makes it one of the most massive disks orbiting a low-mass Class II stellar system. At millimeter wavelength (0.5–3 mm), the various images also reveal that the dust ring is largely smooth and homogeneous, with azimuthal brightness variations below 20%. All three stars have circumstellar disks, but only the single one, GG Tau Aa, is large enough to be detectable at millimeter wavelengths, due to tidal truncation in the Ab1/Ab2 system.

The ring has also been intensively studied at near-infrared (NIR; e.g., Duchêne et al. 2004), and its full 3D orientation is accurately constrained. Brauer et al. (2019) used the Monte Carlo radiative transfer code POLARIS to model the dust scattered-light emission in the H band. By studying the shadows of the inner disks onto the outer ring, they showed that two circumstellar disks (among which that of Aa) are coplanar with the ring, while either Ab1 or Ab2 exhibits a misaligned disk. The northern part of the ring is the near side (Guilloteau et al. 1999).

In order to characterize the dust grain properties, we used ALMA to image the dust ring in polarized emission at 3 and



Original content from this work may be used under the terms of the [Creative Commons Attribution 4.0 licence](#). Any further distribution of this work must maintain attribution to the author(s) and the title of the work, journal citation and DOI.

Table 1
Observations

λ (Frequency) (1)	Date (EB) (2)	Ant. (3)	Baseline (4)	θ_{\max} (5)	Flux and Pol. (6)	Phase (7)	σ_I (8)	$\sigma_{Q,U}$ (9)	θ , PA (10)
0.9 (343.425)	Nov 27 (3)	44	15,1263	1.7	J0510, J0522	J0440	332	23	$0.26 \times 0.20, -32$
3 (97.288)	Oct 23, Nov 27 (6)	47	15,1398	6.7	J0510	J0431	23	6.3	$0.71 \times 0.54, -30$

Note. Columns are: (1) λ : observed wavelength in millimeter and frequency in GHz in parenthesis; (2) Date: observing date in 2018 and number of execution blocks, EB, in parenthesis; (3) Ant.: number of antennas included during the observation; (4) Baseline: projected baseline range with minimum, maximum in meters; (5) θ_{\max} : maximum recoverable scale in arcseconds; (6) Flux and Pol.: flux and polarization calibrators J0510+1800 and J0522-3627; (7) Phase: phase calibrator J0440+1437 and J0431+1731; (8) σ_I : sensitivity of Stokes I in $\mu\text{Jy beam}^{-1}$; (9) $\sigma_{Q,U}$: sensitivity of Stokes Q and U in $\mu\text{Jy beam}^{-1}$; (10) θ : angular resolution in " \times ", PA: position angle of θ in degrees.

1.3 mm. We describe the observations, present the results and then the discussion in this Letter.

2. Observations and Results

2.1. Observations

Data were obtained in project 2018.1.00618.S, using ALMA band 3 and 7 receivers in Cycle 6 in 2018. Each execution block (EB) was calibrated separately in flux, bandpass, and gain. The polarization calibrations were performed after merging the calibrated EBs of each band. The four basebands were set in TDM mode (64 channels on 1.875 GHz with resolution 29.3 MHz). The calibration (bandpass, phase, amplitude, flux) was performed using CASA⁸ v5.4.0. No self-calibration was performed. The uncertainties of the presented polarization position angle are in the range of 4° – 10° . The phase center of the presented images is at $(\alpha, \delta) = (04:32:30.37, +17:31:40.24)$. We only present polarization results when the polarized intensity is above a signal-to-noise ratio of 3.

Table 1 summarizes the observation parameters. The flux of J0440 was 0.265 Jy at 343.425 GHz on November 27. The flux of J0431 was 0.126 Jy and 0.141 Jy at 97.288 GHz on October 23 and November 27, respectively. For the polarization calibration using J0522 and J0510, the derived polarization of J0522 is 5.16% and position angle (PA) of -68.7° at 0.9 mm and of J0510 is 7.2% and PA of 83° at 3 mm, both in agreement with other ALMA measurements.⁹ The 0.9 mm images were done with robust weighting with Briggs parameter 0.5 and tapering parameter of $0''.1$, while the 3 mm images are with robust weighting parameter 0.3. Stokes I images are dynamic-range limited, while all others are close to the expected thermal noise.

2.2. Results

The detected polarization and continuum emission are shown in Figure 1. The continuum emission both at 3 and 0.9 mm reveals a narrow ring peaking at radius $\sim 1''.4$ (210 au), and a peak near the ring center that traces emission from the Aa disk. By fitting an inclined uniform ring model to the Stokes I emission at 0.9 mm, we find a center at $(04:32:30.363, +17:31:40.233)$, an i of 36.4° , and a PA of 7.8° , in agreement with Dutrey et al. (2014). Significant polarization is detected both across the dust ring and toward the Aa peak. Table 2 summarizes the measured properties.

⁸ <http://casa.nrao.edu>

⁹ See the ALMA calibrator catalog: <https://almascience.nrao.edu/alma-data/calibrator-catalogue>.

2.2.1. The Aa Disk

The position angles of the polarization on the Aa peak, $13^\circ \pm 8^\circ$ and $6^\circ \pm 8^\circ$, at 3 mm and at 0.9 mm respectively, are in good agreement and consistent with the rotation axis of the dust ring given above, and the axis of the jet detected in [Fe II] (at 15° , see Figure 2(c); Dutrey et al. 2016). The polarization percentage at 3 mm is $1.4\% \pm 0.4\%$, which is larger than that of $0.60\% \pm 0.04\%$ at 0.9 mm.

2.2.2. The Dust Ring

In the dust ring, the percentages of polarization are different between the two wavelengths. The percentage at 3 mm is relatively homogeneous with an average percentage of $1.2\% \pm 0.1\%$ and a standard deviation of 0.5%. In contrast to that, there is a clear radial variation at 0.9 mm, where the mean percentage is $0.6\% \pm 0.2\%$ with a standard deviation of 0.3% at $r < 1''.85$, which then becomes much larger beyond $1''.85$, being $2.8\% \pm 0.8\%$ with a standard deviation of 1.4%.

The polarization orientation patterns also differ between both wavelengths (see Figures 1(a), (d)). At large radii, $r > 1''.85$, the same azimuthal pattern is revealed at 3 and 0.9 mm. At smaller radii, the pattern remains azimuthal at 3 mm, but becomes almost radial at 0.9 mm. As the angular resolutions of the images at 0.9 and 3 mm are different by a factor of 2.5, we convolved the 0.9 mm images with the resolution of the 3 mm images (not shown), and the flip in polarization remains. This suggests that the difference in polarization at 3 and 0.9 mm is intrinsic.

A closer inspection on the angular separation between the polarization orientation and the tangent to the ellipse at the same radius (using $i = 36^\circ$ and PA = 7°) reveals a systematic deviation (see Figures 2(a), (b), (d), (e) and the histograms of the angular separations in Figures 2(g), (h)). The radial pattern found at 0.9 mm is revealed by a peak at 83° with a standard deviation σ of 16° (i.e., a deviation of -7° with σ of 16° from a purely radial distribution), determined by a Gaussian fit to the histogram, for points with $r < 1''.85$ in Figure 2(g). All the other data points cluster around -8° : Gaussian fits to the histograms yield -9° with σ of 8° at 3 mm and -8° with σ of 10° at 0.9 mm.

At $r < 1''.85$, the 0.9 mm pattern might also be interpreted as aligned with the minor axis, like that of Aa. A Gaussian best-fit to the histogram of the angle differences between the minor axis and the polarization orientation (hereafter, the *parallel model*) indicates a deviation of 6° with σ of 13° (see Figure 2(i)). A good model would lead to Gaussian with σ equal to the typical measurement error for our angles, about 4° to 10° given our signal-to-noise ratio (see Figures 3(a), (b)).

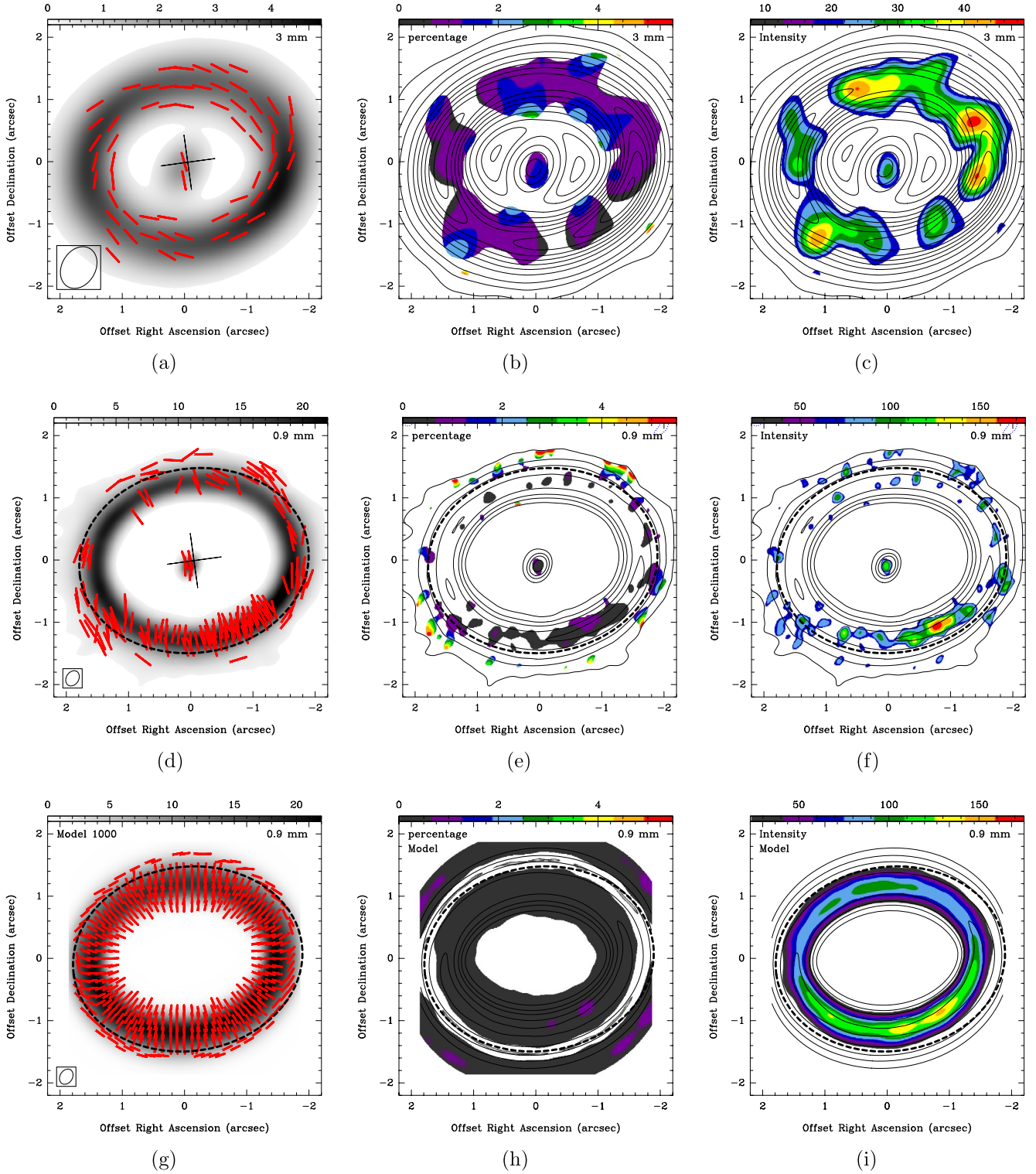


Figure 1. Panels (a), (d): detected polarization position angles shown in red segments and continuum emission in gray scale at 3 and 0.9 mm. Panels (b), (e): polarization percentages in color. Panels (c), (f): polarization intensity in color. The upper and middle panels are results from 3 and 0.9 mm, respectively. Panels (g)–(h) are the model images with a_{\max} of $1000 \mu\text{m}$ at 0.9 mm. The model polarization percentage is masked with a cutoff of 0.2%. Contours in panels (b), (c), (e), (f) denote $-3, 3, 10, 20, 40, 60, \dots, 180, 200 \times \sigma_r$. The wedge units are mJy beam^{-1} in panels (a), (d), (g), percentage in panels (b), (e), (h), and $\mu\text{Jy beam}^{-1}$ in panels (c), (f), (i). The dashed ellipse in panels (d)–(i) marks the $1''.85$ (280 au) radius. Polarization is only displayed for a signal-to-noise ratio in polarized intensity greater than 3.

The σ of the parallel model is 13° , suggesting that this model is not a good representation of the data. Furthermore, the mean deviation in the parallel model is 6° . The alternate hypothesis (angles perpendicular to the ellipse) is not better ($\sigma = 16^\circ$). In

both cases, contamination from the pattern outside $1''.85$ may play a role, and this contamination is largest in the elliptical hypothesis. However, because of the systematic flip of 90° at this radius, while we most measured angles come from the SW

Table 2
Flux of Stokes I and Polarization

Location	Wavelengths	
	3 mm	0.9 mm
Stokes I flux densities in mJy (in K)		
Aa Cont.	2.2 (0.8)	20.9 (3.9)
Ring	56.6	1309.1
Polarization percentage in %		
Aa Cont.	1.4 ± 0.4	0.60 ± 0.04
Ring: $r < 1''.85$	1.2 ± 0.1	0.6 ± 0.2
Ring: $r > 1''.85$	1.2 ± 0.1	2.8 ± 0.8
Gaussian fit deviation of detected PA from ellipse in degrees ^a		
Ring	$-9, \sigma = 8$	$-8, \sigma = 10$
Weighted mean deviation of detected PA from ellipse in degrees ^b		
Ring	-10.0 ± 1.5	-8.0 ± 1.7

Note.

^a The deviation and the standard deviation σ , determined by Gaussian fit, departure from the tangent to an ellipse, at $r > 1''.85$ at 0.9 mm and at all r at 3 mm.

^b The deviation and the standard deviation σ , determined by the weighted mean deviation, departure from the tangent to an ellipse, at $r > 1''.85$ at 0.9 mm and at all r at 3 mm.

part where there is only one measurement that would confuse the parallel hypothesis.

The systematic deviation from the tangent to the ellipse is quantified using the weighted average method following Mori et al. (2019). The weighted average of all the data at 3 mm (Figure 2(e)) is $-10^\circ.0 \pm 0^\circ.8$, with a reduced χ^2 of 3.3. This χ^2 reflects the spatial correlation between points that are separated by less than a beamwidth. Correcting for this correlation leads to the weighted average at 3 mm of $-10^\circ.0 \pm 1^\circ.5$. This value is consistent with that derived from the Gaussian fit to the histogram of angles, although the later is limited by the coarse sampling (5°) and the relatively small number of bins and data points. For 0.9 mm data at $r > 1''.85$, we selected a subset of spatially independent data points from Figure 2(b). The weighted average at 0.9 mm is $-8^\circ.0 \pm 1^\circ.7$, but with a reduced χ^2 of 2.2. This reduced χ^2 is most likely due by spatial contamination from the different pattern at $r < 1''.85$. Combining both bands, our data indicate an angle difference of $-9^\circ.0 \pm 1^\circ.2$ between the polarization vectors and the tangent to the ellipse.

The polarization intensities appear asymmetric between the northern and southern part of the dust ring. At 0.9 mm, the contrast in polarization intensity at $r < 1''.85$ (see Figure 1(f)) is as large as 2.5, calculated using the peak polarization intensity of $173 \mu\text{Jy beam}^{-1}$ in the southeast with respect to the 3σ upper limit of the polarization sensitivity in the northwest, while the contrast in total intensity is only 20% (Figures 1(d), (e)).

At 3 mm we found a similar contrast level in polarization intensity across the dust ring. However, we note that the polarization intensity is maximum at PA of $\sim 300^\circ$, which clearly deviates from the location of the peak total intensity

around 260° (see contours in Figure 1(c)). The polarized and total intensities at 0.9 mm both peak at PA of 230° .

3. Discussion and Conclusion

The flip in polarization angle seen at 0.9 mm is suggestive of self-scattering by (partially) optically thick dust, as initially found in HD 142527 by Kataoka et al. (2016). We explore here in more detail whether this interpretation also applies to GG Tau, presenting a qualitative model of the ring polarization, and discuss the limitations of the various possibilities.

3.1. Central Continuum Peak

The continuum emission at the Aa peak has a raw spectral index of ~ 1.9 , consistent with being due to thermal emission from warm, optically thick dust as mentioned by Andrews et al. (2014). The extrapolated contribution from free-free emission at both wavelengths amounts to $\sim 30 \mu\text{Jy}$ (see Andrews et al. 2014, their Figure 1) and is negligible. While the morphology, with the average polarization aligned along the minor axis, is consistent with the self-scattering model (Kataoka et al. 2015), this model does not predict the very different polarization percentages, $1.4\% \pm 0.4\%$ at 3 mm and $0.60\% \pm 0.04\%$ at 0.9 mm, which differ by a factor of 2.2.

3.2. The Dust Ring

Self-scattering. Following Kataoka et al. (2015), the polarization orientations being radial at smaller radii with a flip to azimuthal at larger radii at 0.9 mm are typical of self-scattering, and hence would allow to estimate the maximum grain size.

To check whether self-scattering could explain the observed images, we produce synthetic polarization images at 0.9 mm and at 3 mm using the code POLARIS (Brauer et al. 2016). The POLARIS model was done using the best known disk parameters of the GG Tau A system derived from multi-wavelength data. It includes a uniform circumterinary ring, aligned with the circumstellar disks around Aa and Ab1, and a misaligned (perpendicular) disk around Ab2. It also assumes a Mathis et al. (1977) dust composition and distribution (see details in Brauer et al. 2019). We varied the maximum grain size from 300 to 1000 μm , and obtained a reasonably good model of $a_{\text{max}} = 1000 \mu\text{m}$, see Figures 1(g), (h), (i) and 3(e), (f), (g). We note that the Brauer et al. (2016) model truncates the dust ring at an outer radius up to $\sim 1''.85$ (accounting for the 150 pc distance), while our Stokes I 0.9 mm image clearly shows a faint shoulder extending up to 350 au. The comparison of the model polarization with observations should be restricted to $r < 1''.85$.

The determined a_{max} of 1000 μm seems consistent with the a_{max} of 1–10 mm from the analysis of a dust spectral energy distribution in the ring by Andrews et al. (2014). The model predicts a dominating radial orientation at $r < 1''.85$ at 1.3 mm and an azimuthal orientation at 3 mm. The modeled polarization has an intensity maximum at a PA of $\sim 225^\circ$ (as a result of the ring's inclination and orientation) and a percentage of about 0.6% at 0.9 mm, in good agreement with the observed properties at $r < 1''.85$.

However, the predicted polarization percentage at 3 mm with a_{max} of 1000 μm would be of the order of $\sim 0.2\%$ (see Figures 3(f), (g)), much smaller than the measured value of $1.2\% \pm 0.1\%$. These self-scattering models, although roughly

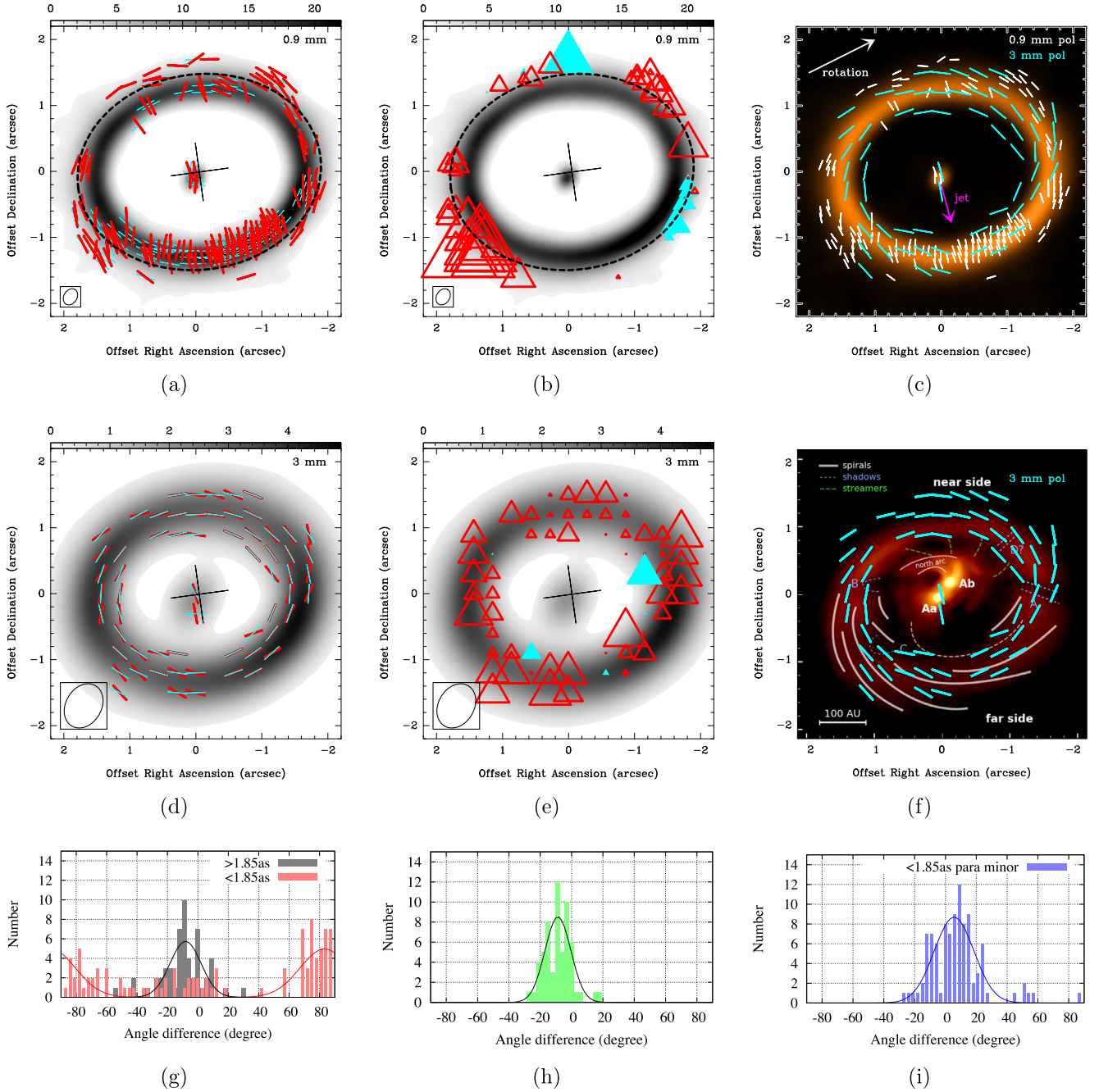


Figure 2. (a), (d) images: Polarization orientations (red segments) and tangents to ellipses (cyan segments) at 3 mm and at 0.9 mm. The cross marks the center of the best-fit uniform dust ring with its orientation. (b), (e): Angle differences between detected polarization orientations and tangents to ellipses for the data at $r > 1''.85$ in (b) and for all the data in (e). Empty triangles denote a negative and solid triangles a positive difference. Larger symbols indicate larger differences. (c) Polarization at 3 mm (cyan segments) and at 0.9 mm (white segments). The orange scale denotes the continuum emission at 0.9 mm. The magenta arrow marks the [Fe II] jet axis. The rotation direction of the circumstellar disk is marked as white arrow. (f): Polarization at 3 mm (cyan segments) overlaid on the spiral patterns revealed at NIR in Kepler et al. (2020). (g), (h), (i) histograms: (g): Histograms of the angle differences defined in panel (b) for the 0.9 mm data, color coded for data at $r > 1''.85$ (black) and at $r < 1''.85$ (red; excluding the Aa disk). The curves are the best-fit Gaussians to the data. (h): The same as in (g) but for the 3 mm data and for all radii. (i): Histogram of the angle differences between the detected polarization orientations and the minor axis of the dust ring for data at $r < 1''.85$ at 0.9 mm.

consistent with the observed pattern at 0.9 mm, fail to reproduce the polarization percentages (and hence the polarization intensity) at 3 mm. Grain properties, such as the grain shape and porosity, can also affect the polarization percentages and orientations, as shown in Kirchschrager et al. (2019) and Kirchschrager & Bertrang (2020). Whether using different grain properties could improve the agreement with the observed polarization requires further investigations.

Magnetic alignment. Guillet et al. (2020) recently investigated the case where dust grains are aligned with toroidal B fields in circumstellar disks. Because of scattering in the Mie regime (when grain sizes are comparable to the observed wavelength, around $\lambda = 2\pi a$), there will be a 90° flip in the polarization angle depending on whether λ is smaller or greater than $2\pi a$. A flip between 3 and 0.9 mm is expected for $a \simeq 250 \mu\text{m}$ (their Figure 2). The model with lognormal size distribution of prolate grains and inclination of 45° (their

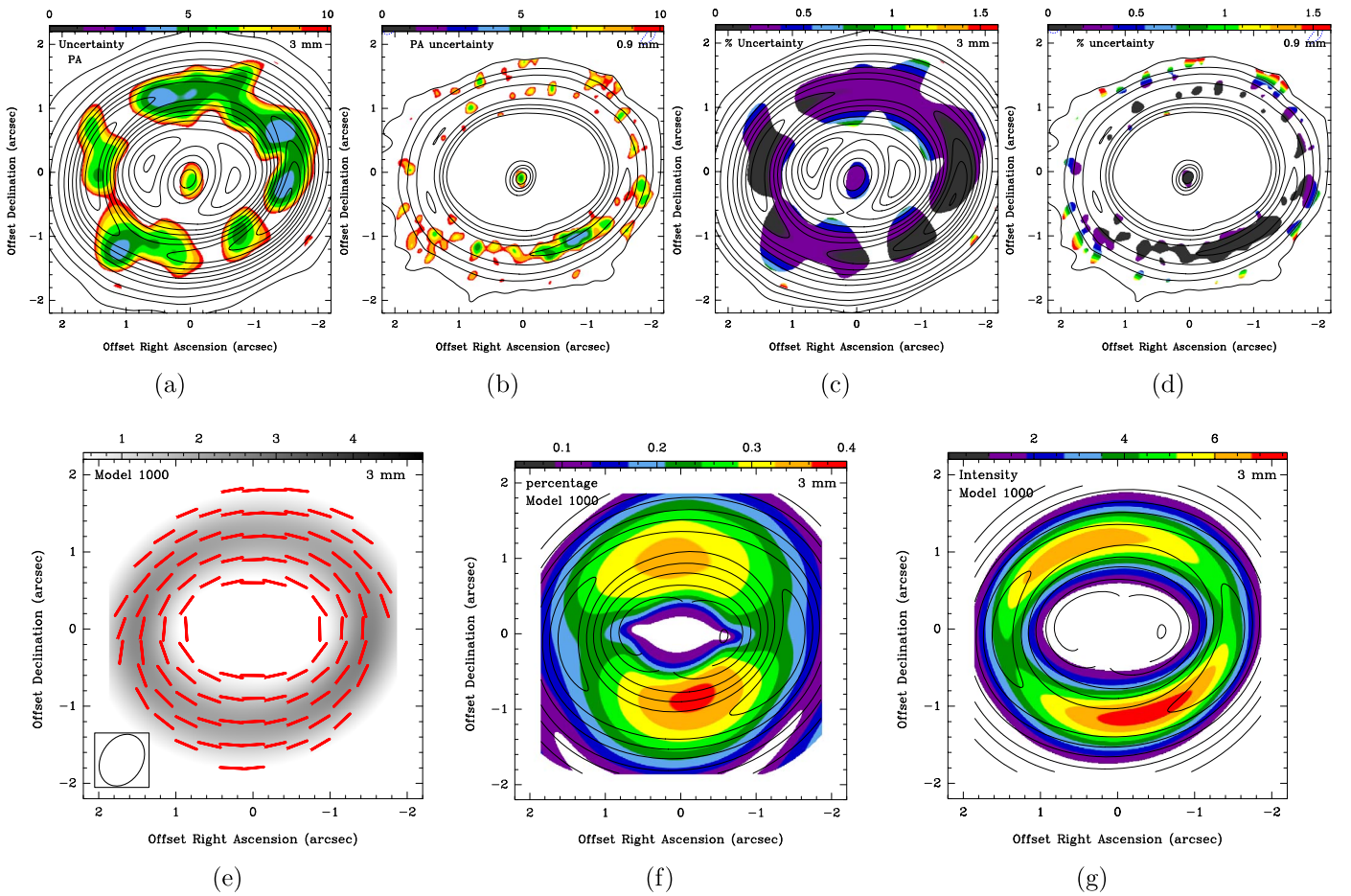


Figure 3. Uncertainty maps of polarization position angle (color scale) in units of degree in panels (a) and (b), and of the polarization uncertainties (color scale) in units of percentage in panels (c) and (d). Contours denote continuum emission. Panels (e), (f), (g): Model images with a_{\max} 1000 μm at 3 mm. Although the azimuthal polarization pattern can be reproduced, the expected polarization percentage of 0.1%–0.4% is much lower than detected (1%–2%). Such a discrepancy is also found in polarization intensity.

Appendix B) with poloidal B fields could qualitatively reproduce the polarization percentages and polarization angles we reported in this letter.

However, neither the self-scattering mechanism nor the magnetic alignment model can explain the systematic deviation of -9° from ellipses observed at both wavelengths. Other possible mechanisms are discussed below:

Mechanical alignment mechanisms? Dust grains with a certain helicity and with a Stokes number around unity can produce leading spiral patterns in polarization position angles (Kataoka et al. 2019). Grains with larger Stokes numbers would not cause any deviation from ellipse, and grains with smaller Stokes numbers would cause radial alignment. Averaged over a grain size distribution, this creates an angle between the polarization and the tangent to the ellipse at any radius. Unfortunately, to reproduce the observed polarization pattern, the GG Tau disk would need to rotate counter-clockwise, in contradiction with the kinematics determined from observations.

A similar deviation (being 4.5°) from ellipses has been also found in AS 209 by Mori et al. (2019) with a coarser angular resolution and also with a rotation direction opposite the expected direction. However, the deviation reported for the GG Tau A system appears at both wavelengths and with more resolved polarization detection.

Spirals? Spirals have been detected in the GG Tau A system in gas (CO observations using ALMA; Phuong et al. 2020) and dust (NIR observations using SPHERE; Keppler et al. 2020) components. They have a different origin: CO spirals are likely due to planet formation in the outer disk, while spirals observed in NIR are due to gravitational interactions with the triple central star. Figure 2(f) reveals that the -9° deviation of the polarization angle is in agreement with the direction of the spiral pattern observed by Keppler et al. (2020). In this case, the -9° would be just the pitch angle of the spirals. However, it is unclear how dust grains could be aligned with these spirals.

Inward grain drift? Yet another possible origin of the -9° deviation of the polarization orientations from the tangents might be that the dust grains are actually drifting inward. In this scenario, the -9° deviation would measure the radial component of the drift motion as a fraction of the (azimuthal, i.e., tangential) Keplerian speed. The findings in favor of such a mechanical alignment (Gold mechanism; Gold 1952) where elongated dust grains would align with the drifting flow and produce polarization are (1) the -9° deviation from ellipses is seen across the entire dust ring at all radii at 3 mm and at $r > 1''.85$ at 0.9 mm; (2) a similar deviation with respect to a radial polarization orientation at $r < 1''.85$ at 0.9 mm; (3) self-scattering can occur superimposed on the mechanical flow alignment. A -9° deviation would amount to 16% of the Keplerian speed. Taking into account the projection due to the

36° inclination, the measured plane-of-sky projected deviation will become about -7.3 when deprojected (Gupta et al. 2022), leading to about 12.8% of the Keplerian speed.

However, to first order the drift velocity of dust grains v_d with respect to the Keplerian velocity v_K is expressed as $v_d/v_K = -(p + q/2 + 3/2) \cdot (c_s/v_K)^2 / (\tau_{\text{fric}} + 1/\tau_{\text{fric}})$, where p and q are the exponents of the surface density and temperature radial profiles respectively, and τ_{fric} is the product of the stopping time and the orbital pulsation (Armitage 2007). The maximum drift velocity occurs for $\tau_{\text{fric}} \equiv 1$. For typical radial profiles, $(p + q/2 + 3/2) \approx 3-4$, and hence $|v_d/v_K| \approx 2 \cdot (c_s/v_K)^2$. Adopting a sound speed of 0.3 km s^{-1} at 20 K and a Keplerian speed of 2 km s^{-1} for the GG Tau ring at 250 au yields a maximum grain drift velocity of 4.5% of the Keplerian speed, corresponding to a deviation of 2°.6. While this could be the first detection of radially drifting dust grains using polarization measurements, the observed values are about a factor of 2.8 larger than the theoretically expected values.

In conclusion, so far there is no satisfactory model of a single mechanism that explains the polarization patterns and percentages. A single wavelength observation is insufficient to unveil the complexity of the polarization mechanisms at work in circumstellar disks. Moreover, both the polarization patterns and percentages at several wavelengths must be reproduced.

This project is supported by the Ministry of Science and Technology (MoST) in Taiwan. Y.W.T. acknowledges support through NSTC grant NSTC 110-2112-M-035- and NSTC 111-2112-M-001-064-. P.M.K. acknowledges support through NSTC grant NSTC 110-2112-M-001-057- and NSTC 111-2112-M-001-070-. This paper makes use of the following ALMA data: ADS/JAO.ALMA#2018.1.00618.S. ALMA is a partnership of ESO (representing its member states), NSF (USA) and NINS (Japan), together with NRC (Canada), MOST and ASIAA (Taiwan), and KASI (Republic of Korea), in cooperation with the Republic of Chile. The Joint ALMA Observatory is operated by ESO, AUI/NRAO and NAOJ. This work was supported by the French ‘‘Programme National de Physique Stellaire’’ (PNPS) of CNRS/INSU co-funded by CEA and Programme National de Planétologie (PNP) of CNRS/INSU co-funded CNES.

ORCID iDs

Ya-Wen Tang  <https://orcid.org/0000-0002-0675-276X>
 Patrick M. Koch  <https://orcid.org/0000-0003-2777-5861>
 Stephane Guilloteau  <https://orcid.org/0000-0003-3773-1870>
 Hsi-Wei Yen  <https://orcid.org/0000-0003-1412-893X>
 Emmanuel di Folco  <https://orcid.org/0009-0009-9618-4927>
 Eric Pantin  <https://orcid.org/0000-0001-6472-2844>
 Akimasa Kataoka  <https://orcid.org/0000-0003-4562-4119>

References

- Andrews, S. M., Chandler, C. J., Isella, A., et al. 2014, *ApJ*, 787, 148
 Armitage, P. J. 2007, arXiv:astro-ph/0701485
 Brauer, R., Pantin, E., Folco, E. D., et al. 2019, *A&A*, 628, A88
 Brauer, R., Wolf, S., & Reissl, S. 2016, *A&A*, 588, A129
 Di Folco, E., Dutrey, A., Le Bouquin, J.-B., et al. 2014, *A&A*, 565, L2
 Duchêne, G., McCabe, C., Ghez, A. M., & Macintosh, B. A. 2004, *ApJ*, 606, 969
 Dutrey, A., Folco, E. D., Beck, T., & Guilloteau, S. 2016, *A&ARv*, 24, 33
 Dutrey, A., Folco, E. D., Guilloteau, S., et al. 2014, *Nature*, 514, 600
 Dutrey, A., Guilloteau, S., & Simon, M. 1994, *A&A*, 286, 149
 GAIA collaboration, Brown, A. G. A., Vallenari, A., et al. 2018, *A&A*, 616, A1
 Gold, T. 1952, *MNRAS*, 112, 215
 Guillet, V., Girart, J. M., Maury, A. J., & Alves, F. O. 2020, *AA*, 634, L15
 Guilloteau, S., Dutrey, A., & Simon, M. 1999, *A&A*, 348, 570
 Gupta, A., Yen, H.-W., Koch, P., et al. 2022, *ApJ*, 930, 67
 Kataoka, A., Muto, T., Momose, M., Tsukagoshi, T., & Dullemond, C. P. 2016, *ApJ*, 820, 54
 Kataoka, A., Muto, T., Momose, M., et al. 2015, *ApJ*, 809, 78
 Kataoka, A., Okuzumi, S., & Tazaki, R. 2019, *ApJL*, 874, L6
 Kataoka, A., Tsukagoshi, T., Pohl, A., et al. 2017, *ApJL*, 844, L5
 Keppler, M., Penzlin, A., Benisty, M., et al. 2020, *A&A*, 639, A62
 Kirchschlager, F., & Bertrang, G. H.-M. 2020, *A&A*, 638, A116
 Kirchschlager, F., Bertrang, G. H.-M., & Flock, M. 2019, *MNRAS*, 488, 1211
 Mathis, J. S., Rumpl, W., & Nordsieck, K. H. 1977, *ApJ*, 217, 425
 Mori, T., Kataoka, A., Ohashi, S., et al. 2019, *ApJ*, 883, 16
 Phuong, N. T., Dutrey, A., Folco, E. D., et al. 2020, *A&A*, 635, L9
 Piétu, V., Gueth, F., Hily-Blant, P., Schuster, K.-F., & Pety, J. 2011, *A&A*, 528, A81
 Tazaki, R., Lazarian, A., & Nomura, H. 2017, *ApJ*, 839, 56
 Yang, H., Li, Z.-Y., Stephens, I. W., Kataoka, A., & Looney, L. 2018, *MNRAS*, 483, 2371